X-ray absorption spectroscopy study of the Li$_x$FePO$_4$ cathode during cycling using a novel electrochemical *in situ* reaction cell

Aniruddha Deb,[a]* Uwe Bergmann,[b] Elton J. Cairns[a,c] and S. P. Cramer[d,e]

[a]*Environmental Energy Technologies Division, Lawrence Berkeley National Laboratory, Berkeley, CA 94720, USA,* [b]*Stanford Synchrotron Radiation Laboratory, Sand Hill Road, Menlo Park, CA 94025, USA,* [c]*Department of Chemical Engineering, University of California, Berkeley, California, USA,* [d]*Physical Bioscience Division, Lawrence Berkeley National Laboratory, Berkeley, CA 94720, USA, and* [e]*Department of Applied Sciences, University of California, Davis, California, USA. E-mail: adeb@lbl.gov*

The extraction and insertion of lithium in LiFePO$_4$ has been investigated in practical Li-ion intercalation electrodes for Li-ion batteries using Fe K-edge X-ray absorption spectroscopy (XAS). A versatile electrochemical *in situ* reaction cell was utilized, specifically designed for long-term X-ray experiments on battery electrodes during the lithium-extraction/insertion process in electrode materials for Li-ion batteries. The electrode contained about 7.7 mg of LiFePO$_4$ on a 20 µm-thick Al foil. In order to determine the charge compensation mechanism and structural perturbations occurring in the system during cycling, *in situ* X-ray absorption fine-structure spectroscopy (XAFS) measurements were conducted on the cell at a moderate rate using typical Li-ion battery operating voltages (3.0–4.1 V *versus* Li/Li$^+$). XAS studies of the LiFePO$_4$ electrode measured at the initial state (LiFePO$_4$) showed iron to be in the Fe(II) state corresponding to the initial state (0.0 mAh) of the battery, whereas in the delithiated state (FePO$_4$) iron was found to be in the Fe(III) state corresponding to the final charged state (3 mAh) of the battery. The X-ray absorption near-edge structure (XANES) region of the XAS spectra revealed a high-spin configuration for the two states [Fe(II), d^6 and Fe(III), d^5]. The XAFS data analysis confirmed that the olivine structure of the LiFePO$_4$ and FePO$_4$ is retained by the electrodes, which is in agreement with the X-ray diffraction observations on these compounds. The XAFS data that were collected continuously during cycling revealed details about the response of the cathode to Li insertion and extraction. These measurements on the LiFePO$_4$ cathode show that the material retains good structural short-range order leading to superior cycling.

1. Introduction

Li-ion batteries are of much interest for electrochemical energy storage systems (Haas & Cairns, 1999). During operation of the battery, the electrode materials are subjected to oxidation and reduction processes. These processes result in an electric current between the electrodes, allowing us to draw power from the battery. There have been numerous efforts to observe the detailed changes that occur in and on the electrodes during the charging and discharging process. In the case of the modern Li-ion batteries, the electrode materials permit lithiation and delithiation, a mechanism that in the long run can result in severe degradation of the electrodes and hence limit the life of the battery. Real-time tracking of the changes in the electrode materials undergoing electrochemical reactions is best performed by utilizing an *in situ* cell reaction chamber. The advantage of *in situ* XAS measurements lies in the ability to directly monitor detailed structural changes in the electrode material as ion extraction/insertion proceeds. This, along with the electrochemical measurements, provides us with valuable information about the relationship between structure and electrochemical properties, which is not accessible from *ex situ* experimental measurements. Since 1990, interest in Li-ion batteries has increased dramatically owing to the large demand of small powerful sources for mobile electronic devices such as cell phones and laptops. Higher specific energy as well as higher cell voltages are the desirable key features, whereas capacity fading and possible environmental hazards are to be minimized. The investigations in this field have mostly been carried out by X-ray diffraction techniques performed *ex situ* as well as *in situ* (Richard *et al.*, 1997; Etgens *et al.*, 1999; Palacin *et al.*, 1999). There have been a number of X-ray *in situ* chambers that have been designed to study the reaction mechanism in battery electrodes. The main challenges of X-ray measurements on battery materials are sample inhomogeneities in the case of transmission studies and corrosion if the sample is exposed to ambient conditions. In particular, for the alkali-metal-based systems like the lithium batteries, adequate sealing of the cell plays a very important role for the *in situ* investigations. Therefore, in both transmission and fluorescence mode, for *in situ* X-ray absorption measurements the appropriate cell designs have been crucial. For the work reported here we constructed a novel *in situ* cell, simple in design, for easy assembly in a glove box. Furthermore, the device is portable, re-usable and has effective sealing so that the experiments can run for several days without any degradation of the electrodes when the cell is exposed to ambient atmosphere. A detailed description is given below.

Since the demonstration of reversible electrochemical lithium extraction/insertion for LiFePO$_4$ (Padhi *et al.*, 1997), lithium transition-metal phosphates with ordered olivine structure have attracted much attention as a promising new cathode material for rechargeable Li batteries. LiFePO$_4$ has a theoretical specific capacity of 170 mAh g^{-1} and a voltage of >3.4 V *versus* Li/Li$^+$. LiFePO$_4$ is inexpensive, non-toxic, non-hygroscopic and environmentally friendly. It occurs in nature as the mineral triphylite, which has an orthorhombic unit cell (space group *Pnma*) (Streltsov *et al.*, 1993). Both Li and Fe atoms are in octahedral sites with Li located in the 4a and Fe in the 4c positions. The O atoms are nearly hexagonal closed-packed and the Fe atoms occupy zigzag chains of corner-shared octahedra running parallel to the *c* axis in alternate *a*–*c* planes. These chains are bridged by corner- and edge-sharing (PO$_4^{3-}$) polyanions to form a host structure with strong three-dimensional bonding. The Li$^+$ ions in the 4a sites form continuous linear chains of edge-shared octahedra running parallel to the *c* axis in the other *a*–*c* planes. The P$_{tet}$–O–Fe$_{oct}$ linkage in the structure induces a super-exchange interaction that tunes the Fe^{3+}/Fe^{2+} redox energy to useful levels (3.4 V) (Padhi *et al.*, 1997). The stable nature of the olivine-type structure having a (PO$_4^{3-}$) polyanion with a strong P—O covalent bond provides not only excellent cycle life but also a safe system. The fact that all O atoms are not only bonded to Fe but also strongly bonded to phosphorous is advantageous for the safety of the battery since oxygen is less likely to be released at elevated temperature, which makes oxygen ignition of the organic electrolyte an unlikely accident. Low utilization owing to conductivity problems within the electrode and slow electron transfer kinetics at the iron phosphate retarded its application to start with (Yang *et al.*, 2002). Special

coatings, small grain size and substitution of part of the iron by other metals are concepts to ameliorate these unattractive properties (Chung *et al.*, 2002; Yang *et al.*, 2003; Ravet *et al.*, 2001). When the electrode is fully charged, the reactivity with regard to the combustion reaction with the organic electrolyte is low (Yamada & Chung, 2001). Until now, to our knowledge, X-ray absorption spectroscopy has not been used to investigate this electrode material but similar compounds of hexaoxygen-coordinated iron compounds (Westre *et al.*, 1997; Manceau *et al.*, 2000) have been studied by this method.

Furthermore, very few studies exist where *in situ* cells have been used for experiments extending for several days or even a week. Owing to the known limitations of *in situ* investigations, *e.g.* difficult cycling set-up and complicated multi-element assembly of a working cell, these experiments are more complicated compared with *ex situ* measurements. Some alternative methods have been developed that use cycling and disassembling of the cells under appropriate electrochemical conditions. However, in this case only a post mortem analysis is possible, with the risk that the material is substantially altered from its conditions during the reaction. After overcoming many obstacles, Ronci *et al.* (2001) recently reported an *in situ* X-ray study using energy-dispersive X-ray diffraction (EDXD), where the instrumental set-up enabled them to perform long-lasting data acquisitions. The use of industrial *in situ* cells (Richard *et al.*, 1997) is reported in an X-ray diffraction (XRD) study (Gerand *et al.*, 1999) wherein the device for the XRD analysis was used on a Guinier–Lenne geometry camera; here the focused monochromatic beam passed through the plastic Li-ion cell protected by a metal–plastic laminate.

Upon charging and discharging a cell, the lithium ions are extracted and inserted from the electrode material. This reaction is seriously limited by diffusion and may take hours. Some of the changes in the electrode material may occur only after a large number of charge and discharge cycles, hence the experiments can last as long as several weeks or even months. It is also important to note that, when lithium is exposed to the ambient atmosphere, lithium reacts with the nitrogen of air and forms lithium nitride, while, with the humidity present in air, lithium reacts to form lithium hydroxide. The electrolytes used in the battery sometimes form corrosive end products when they come into contact with air. Hence, to minimize these corrosive reactions, the batteries are designed to be completely sealed. Usually the battery test cells that are used for *in situ* measurements satisfy these sealing requirements and hence allow the cycling measurements to continue for months. On the contrary, *in situ* measurements using X-rays require X-ray windows, and hence are more prone to leakage. To prevent these *in situ* cells from leaking, some of the cells use extensive sealants, but these often work for single time use only.

In the studies reported here we use a novel reusable *in situ* cell. It utilizes kapton X-ray windows, is convenient to assemble in the glove box and is portable. The effective design of the *in situ* cell allows us to cycle the cell for several weeks without any noticeable traces of corrosion of the lithium metal counter electrode. Furthermore, the cell was designed so that it can be used for measurements at both the hard and soft X-ray sources and for different techniques like XAS, small-angle X-ray scattering (SAXS) and small-angle X-ray diffraction. The cell was used for the XAS study of lithium-extraction/insertion from Li_xFePO_4 electrodes. Both Fe *K*-edge X-ray absorption near-edge structure (XANES) and extended X-ray absorption fine structure (EXAFS) techniques were applied. In contrast to *in situ* XRD, which provides a good picture of the long-range structural changes in the electrode, XAS provides detailed information of the electronic structure (oxidation state) as well as short-range ordering,

which may not be accessible from XRD. An *in situ* examination of the structure of the electrode material Li_xFePO_4 with XAFS during cycling can be illuminating in its own right, but also provides a baseline for further studies in which the electrode material is modified by the introduction of additional elements.

2. Design of the *in situ* cell

The cell design and a photograph of the complete assembled cell are shown in Fig. 1. A schematic drawing of the cylindrical cell is shown in Fig. 1(*a*). The cell mainly consists of six parts (labelled as A–F). The main support of the cell is provided by the two stainless steel discs A and B (80 mm in diameter). The central region of parts A and B is the sample compartment (or chamber) which hosts the working electrode sample (in this case Li_xFePO_4, 20 mm in diameter), the ion-conducting separator (from Celgard) soaked in electrolyte, and a lithium metal counter electrode (as shown in Fig. 1*a*). The lithium electrode serves as both the counter and the reference electrode. This is possible because the lithium electrode has a very high exchange current density and also due to the very low current densities used for operation of the cell, and exhibits the reversible potential under all of the conditions used. It is well known from other experiments in this laboratory and others that stainless steel is not corroded by the contents of these cells. In the sample compartment of part A of this assembly of the working electrode, the separator and the lithium counter electrode are placed on a stainless steel metal base (part F, 3 mm thickness). This metal plate protects the kapton X-ray window
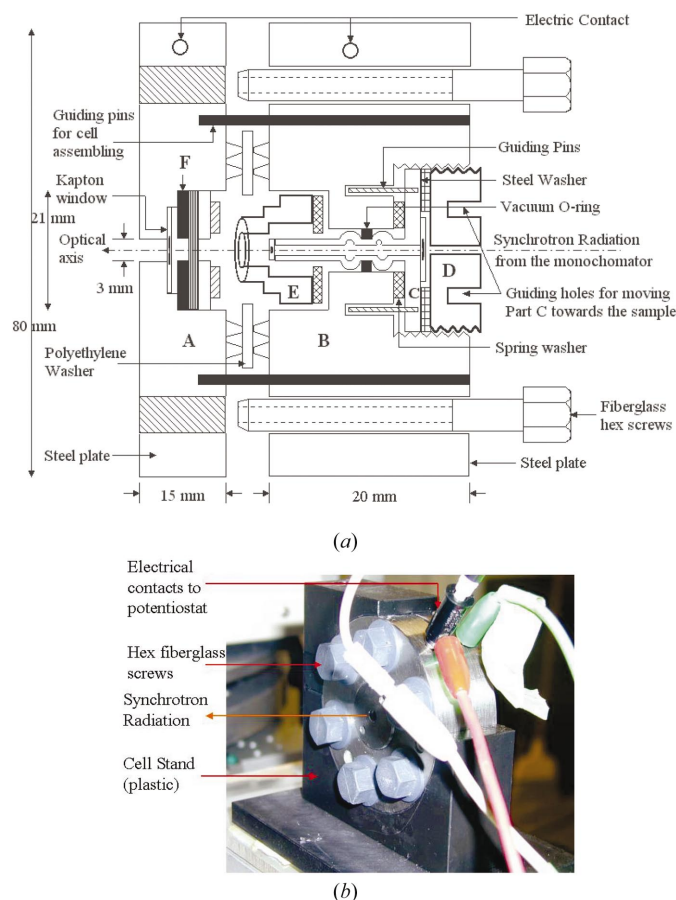

Figure 1
(*a*) Cross-sectional view of the *in situ* electrochemical cell. (*b*) Photograph of the *in situ* reaction cell, at the beamline, with part B facing.

from becoming damaged. The X-ray windows at the centre of A and B are 3 mm in diameter. Part B is designed in such a way that it accommodates parts C and D from outside. Part C consists of a stainless steel base with a central 3 mm X-ray window that goes inside part B. The long stem of part C that goes inside part B carries a vacuum O-ring. Sealing of the cell is crucial to prevent the electrolyte from drying out and to prevent the lithium foil counter electrode and the sample from chemical reactions with the ambient atmosphere. We have carried out a systematic study on how many vacuum O-rings are necessary to provide sufficient protection. We have tested single and double vacuum O-rings and found that a single vacuum O-ring was clearly sufficient for proper sealing and is still efficient and feasible in terms of cell machining and design. Inserting two vacuum O-rings on the long stem of part C unnecessarily makes part B much thicker and the stem of part C longer to accommodate the two O-rings. On the side of part C that faces the electrode assembly, the window is sealed by 0.005 cm-thick kapton foil, while at the base of part C from outside we have sealed the X-ray window with 0.005 cm-thick kapton foil. This was mainly designed to achieve a better and a more effective sealing of the cell. To protect the Kapton foil from being damaged a steel washer was placed at the base of part C. The two guiding pins on part C help it to be inserted into part B without damaging the vacuum O-ring. Part D is then screwed inside part B with the help of the two guiding holes. Furthermore, at the base of part C we have placed a spring washer, separating parts B and C, such that the X-ray window of part C can be moved closer to or farther from the sample electrode by about 2 mm by tightening or loosening part D, which holds part C tightly with part B. Part E is designed in such a way that it fits tightly inside part B, and has a central X-ray window (3 mm in diameter) for the X-ray beam to pass through the cell. At the base of part E there is a spring washer, which helps to keep the sample assembly in the sample compartment tight with adequate pressure. Between the steel discs A and B there is a polyethylene washer (with external diameter 40 mm and internal diameter 17 mm) that provides an efficient way of sealing the sample compartment from the ambient atmosphere. We have also tested a polypropylene washer of similar dimensions, but the polyethylene washer was seen to provide better sealing.

Thus in the sample compartment the working electrode is in direct contact with the steel disc A while the counter electrode is in contact with disc B. The electrical contacts present in the steel discs A and B are then connected to the potentiostat (using banana plugs) for charging and discharging the electrochemical cell. The cell assembly was found to be stable for more than a week without any noticeable traces of corrosion of the lithium metal. Fig. 1(b) shows a photograph of the assembled cell at the beamline during measurements, showing the face of the steel disc B. During the experimental run the cell performed well without any significant contamination or corrosion for more than a week of exposure to the ambient atmosphere.

3. Experimental

3.1. Cell assembly

The experiments were performed with a complete lithium/iron phosphate cell. The $LiFePO_4$ powder was synthesized using the starting materials $Fe(NO_3)_3 \cdot 9H_2O$ (iron nitrate, Aldrich, 99.99%), $Li(CH_3COO)_2 \cdot 2H_2O$ (lithium acetate, Aldrich, 99%), H_3PO_4 (phosphoric acid, Sigma) and $HOCH_2COOH$ (glycolic acid, Aldrich). The metal compounds were first dissolved in phosphoric acid and then in de-ionized water. This solution was mixed until homogenous, and was added to glycolic acid (where the metal:glycolic acid ratio is 1:2). Ammonium hydroxide was added to the solution to adjust the pH to between 8.5 and 9.5. The solution was heated to 343–353 K under

nitrogen until a gel was formed. This gel was then transferred to an alumina boat, heated slowly to 773 K under flowing nitrogen, and then decompressed at that temperature for about 10 h. The resultant powders were ground, dried and then heated to 873 or 973 K under a flow of nitrogen gas for 5–15 h [see Doeff et $al.$ (2003) for details of the preparation]. The product was a single phase, as was verified by XRD. The electrodes were cast on an aluminium foil of thickness 25 μm, containing the powdered cathode material, Kynar PVdF binder (KynarFlex 2801, Atochem), SFG-6 synthetic flake graphite (Timrex Timcal) and compressed acetylene black (laminated electrodes contain 80 wt% active material, 8 wt% Kynar PVdF binder, 6 wt% SFG-6 synthetic flake graphite and 6 wt% compressed acetylene black). Electrodes with a 20 mm diameter were punched from the foil sheet. A separator (from Celgard, Celgard 3400) with an outer diameter of 20 mm and an inner diameter of 4 mm (Fig. 1a) was punched from the separator sheet. Before taking the cell parts inside the glove box, parts C and E were fixed in part B of the cell. Then all necessary cell parts, chemicals and tools for the assembly were placed in an argon-filled glove box in the laboratory. Our cell was designed so that it was very easy to assemble in the glove box. First, the working electrode (Li_xFePO_4) was placed on the metal plate (F), then the separator was placed on top of the working electrode. The separator was soaked with electrolyte, 1 M $LiPF_6$ dissolved in 50 wt% ethylene carbonate (EC) and 50 wt% dimethylcarbonate (DMC) obtained as a solution from Merck. The electrode contained about 8 mg cm^{-2} $LiFePO_4$ on the 25 μm-thick Al foil. A piece of lithium foil counter electrode was then punched with an outer diameter of 14 mm and an inner diameter of 6 mm (Fig. 1a) from fresh supplies and placed on top of the separator. Finally, a polyethylene washer was placed on top of the lithium foil counter electrode, and part B (with part E in place) was placed on part A (with all necessary battery cell parts in the sample compartment) using the guiding pins. The fiberglass hex screws were then used to tighten parts A and B together (Fig. 1b). A computer-controlled Princeton Applied Research Model VERSA potentiostat/galvanostat was used for cycling the electrochemical cell under constant current control.

3.2. Electrochemical cycling of the Li_xFePO_4 electrode

Electrochemical cycling of the cell was performed at a constant current density of 1 mA cm^{-2} between 4.1 and 2.9 V, which corresponds to a 3.0 h rate. The voltage–time curve in Fig. 2 shows a plateau at about 3.5 V whereas the discharge exhibits a similar curve with a plateau at about 3.4 V. In Fig. 2, 3.2 V represents the open circuit potential at the fully lithiated state. Other electrochemical experiments with cells of this type indicate excellent stability at open circuit, and negligible rates of self discharge.

3.3. X-ray absorption measurements

The XAS studies were performed on the insertion-device undulator beamline of the Materials Research Collaborative Access Team (MR-CAT, sector 10) and the bending-magnet beamline of DND-CAT (5-BM-D) at the Advanced Photon Source (APS), Argonne National Laboratory, USA. We used the Si(111) reflection from a cryogenically cooled double-crystal monochromator with an energy resolution of ∼1 eV, as measured by the rocking-curve width of the second crystal. An active feedback loop was used to maintain the peak reflectivity of the monochromator. The large harmonic content in the beam was rejected by employing a platinum-coated mirror (Segre et $al.$, 2000). The energy cut-off of the mirror was around 20 keV. All the measurements were recorded in the transmission mode using three ion chambers in series to measure the intensities of
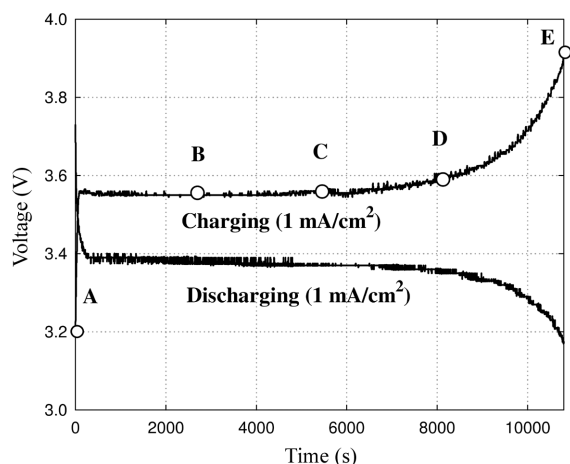
Figure 2
The voltage–time charging (delithiation, $LiFePO_4 - e \rightarrow FePO_4 + Li^+$) and discharging (lithiation) curve for $LiFePO_4$ using the *in situ* cell; the cut-off limit was 4.0–4.1 V. The discharge cut-off limit was 2.9 V. A (0 mAh), B (0.75 mAh), C (1.5 mAh), D (2.25 mAh) and E (3.0 mAh) in the figure mark the different stages in the charge process at which the XAS measurements were performed. States A, B, C, D and E are shown in the charging curve.

the incident beam I_0, the beam transmitted by the sample I_t and the beam subsequently transmitted by the reference foil I_{ref}. The I_0 chamber was filled with a mixture of helium/nitrogen (80/20%), while the I_t and I_{ref} chambers were filled with nitrogen. A beam size of 0.8 mm × 0.8 mm was chosen and the resulting incident-beam flux was $\sim 10^{11}$ photons s^{-1}. An Fe metal foil was used to calibrate the energy at the edge. To achieve time resolution suitable to follow the electrochemical reaction, the EXAFS scans were performed in continuous mode (with data collection during the monochromator movement) (Frahm, 1988). This reduced the acquisition time per scan to about 9 min by eliminating the time required to step the monochromator. The monochromator was scanned in energy from 200 eV below to 800 eV above the Fe K absorption edge (7112 eV). Increasing the measurement speed enabled us to maintain an approximately constant current in the electrochemical cell for the duration of a cycle, and there was no need to interrupt the current to take long EXAFS measurements. It has been shown previously that such fast continuous EXAFS scans during cell operation are better suited for observing electrochemically driven reactions, as compared with reducing the cell current to near zero during measurement (Mansour *et al.*, 1999). A faster measurement time enables us to achieve much greater detail concerning the composition and structural parameters as a function of the cell potential. The reduction of the absorption data was performed using *ATHENA* (Newville, 2001) and the *EXAFSPAK* analysis package (available from SSRL at http://www-ssrl.slac.stanford.edu/exafspak.html).

4. Results and discussion

The structure of $LiFePO_4$ has been investigated by different groups (Huang *et al.*, 1998; Yamada, Chung & Hinokuma, 2001). Our XRD investigation of the $LiFePO_4$ electrode showed the typical XRD pattern expected for olivine-structured $LiFePO_4$. The atomic structure fits to the space group symmetry *Pnma* (#62). By using the *Powdercell2.4* program (http://www.ccp14.ac.uk/ccp/web-mirrors/powdcell/a_v/v_1/powder/e_cell.html) and utilizing the atomic positions listed in Table 1, the atomic structure of the $LiFePO_4$ can be visualized as shown in Fig. 3, where the atomic distances are also indicated. The structure shown in Fig. 3 shows four $LiFePO_4$ units; the

Table 1
Crystal coordinates of the atoms of $LiFePO_4$ ($\alpha = \beta = \gamma = 90°$ at $T = 293$ K).

	a (Å)	b (Å)	c (Å)
	10.3320	6.010	4.6920
Atom	x	y	z
Li	0.0	0.0	0.0
Fe	0.2822	0.25	0.9747
P	0.0949	0.25	0.4182
O(1)	0.0968	0.25	0.7428
O(2)	0.4571	0.25	0.2060
O(3)	0.1656	0.0465	0.2848

O sites form an approximately tetrahedral arrangement around the phosphorus sites and a distorted octahedral arrangement of the phosphate O atoms around each Fe site. The distortion reduces the symmetry from O_h to C_s symmetry (Yamada, Chung & Hinokuma, 2001). The positions of the oxygen sites are shown in Table 1, and the Fe—O distances vary by almost 0.2 Å. There are three different positions and four different interatomic Fe—O distances (2 × 2.2506 Å equatorial, 2 × 2.0639 Å equatorial, 1 × 2.2034 Å axial, 1 × 2.1077 Å axial) (Streltsov *et al.*, 1993; Yakubovich *et al.*, 1977). The mobile Li^+ ions are accommodated in the two-dimensional Li channel along the *a* and *b* axes. On charging, the Li ions are removed electrochemically and the remaining $FePO_4$ retains the same *Pnma* symmetry with approximately 7% reduced volume (Huang *et al.*, 1998; Andersson & Thomas, 2001). The charging and discharging curves, shown in Fig. 2, were obtained by charging and discharging the electrochemical cell with a constant current density of 1 mA cm^{-2}, which corresponds to a 2–3 h charging and discharging rate. As shown in Fig. 2, EXAFS measurements were taken at the points marked as A (0.0 mAh), B (0.75 mAh), C (1.5 mAh), D (2.25 mAh) and E (3.0 mAh). For the X-ray absorption near-edge spectroscopy (XANES), we calibrated each scan using the corresponding metal foil reference scan taken simultaneously with the cell data. The calibration procedure was a qualitative best matching of the entire near-edge region of the reference foil scans to one scan in the cell series chosen as the baseline. Even though the energy resolution of the X-ray beam was about 1.0 eV and the step size in the edge region was only 0.5 eV, shifts as small as 0.1 eV were reliably detected by this calibration method. Absolute energy calibration was made to
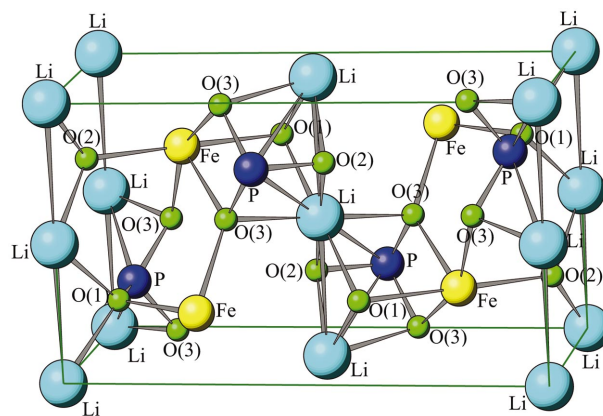

Figure 3
The olivine structure of $LiFePO_4$/triphylite (space group *Pnma*) calculated using *Powdercell2.4*, utilizing the atomic positions shown in Table 1. The corresponding interatomic distances (Å) obtained are: Li—O(1) 2.171; Li—O(2) 2.087; Li—O(3) 2.189; Fe—O(1) 2.203; Fe—O(2) 2.108; Fe—O(3) 2.064; Fe—O(3) 2.250; P—O(1) 1.523; P—O(2) 1.538; P—O(3) 1.556; Li—Li 3.005; Li—P 2.659.

the Fe foil reference scan, assigning energy of 7112 eV to the maximum derivative. The XANES spectra at the Fe K edge (with an edge jump of ~1) during charge (delithiation) are shown in Fig. 4(a), where the edge position of the first five scans shifts to higher energies. Fig. 4(b) shows the pre-edge region of the XAS spectra, which are observed at the stages A and E during the charging process representing the LiFePO$_4$ and the FePO$_4$ phases, respectively. From Fig. 4(a) it is seen that a strong shift of the main edge from stage A to E (about 4 eV) is observed, which is attributed to the change in valence state of iron in the sample during the charging process. This shift of the main edge from the charging state A to E can be explained by screening effects on the 1s electron leading to a stronger bond in the Fe(III) state than in the Fe(II) state. The dipole forbidden pre-edge transitions attributed to Fe 1$s \rightarrow$ 3d bands are also shown in Fig. 4(b). The ligand field resulting from the phosphate O atoms, which are octahedrally coordinated to Fe, split the 3d states into t_{2g} and e_g states. One can expect additional splitting of these states as the O atoms deviate from the normal octahedral coordination (the Fe—O distances change by about 0.2 Å). Hence the observed splitting of the 3d states can be assigned to crystal field splitting of the t_{2g} and e_g energy levels. The energy difference between the t_{2g} and e_g bands is about 2 eV, which is consistent for octahedral oxygen-coordinated transition-metal compounds (Pouchard et $al.$, 2001). The intensity of the pre-edge for the sample in the oxidized state E is similar to that

for the sample in state A, indicating that the O atoms retain the octahedral coordination.

XANES spectroscopy is a powerful technique in characterizing oxidation states and local symmetries of transition-metal ions (Bianconi, 1988), especially when appropriate model compounds, with well defined oxidation and coordination states, are available for comparison. Here we have measured FePO$_4$ as an example of Fe(III) in tetrahedral coordination and α-Fe$_2$O$_3$ and Fe(acac)$_3$ as examples of Fe(III) in octahedral symmetry. FeCp$_2$ has been chosen as an example of a Fe(II) compound (Cp = cyclopentadienyl, acac = acetylacetonate). FePO$_4$ is usually considered as a perfect model for Fe in tetrahedral coordination (Ng & Calvo, 1975), while FeCp$_2$ is a known stable sandwich compound. The X-ray structure of ferrocene indicated a molecular center of symmetry (Eiland & Pepinsky, 1952) (D_{5d} symmetry). Fig. 5(a) shows the XANES spectra of the four model compounds. The three compounds containing ferric species are observed to exhibit a K edge at significantly higher energy (7122.3–7123.2 eV) with respect to FeCp$_2$ (7119.3 eV). The exact edge position is also dependent on the coordination ligands and their local symmetry around the absorbing atom [explaining the observed small difference of <0.1 eV, among FePO$_4$, Fe$_2$O$_3$ and Fe(acac)$_3$]; the main underlying factor which determines the energy required to induce the
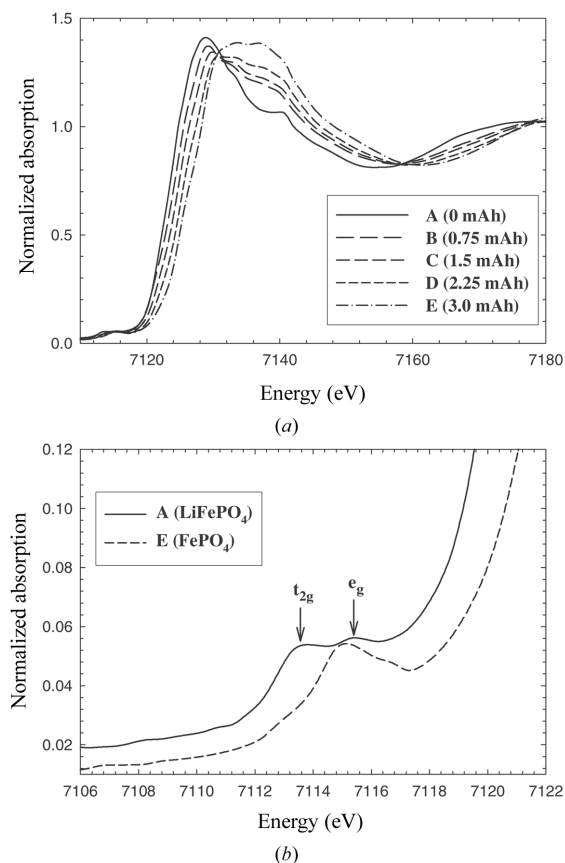

Figure 4
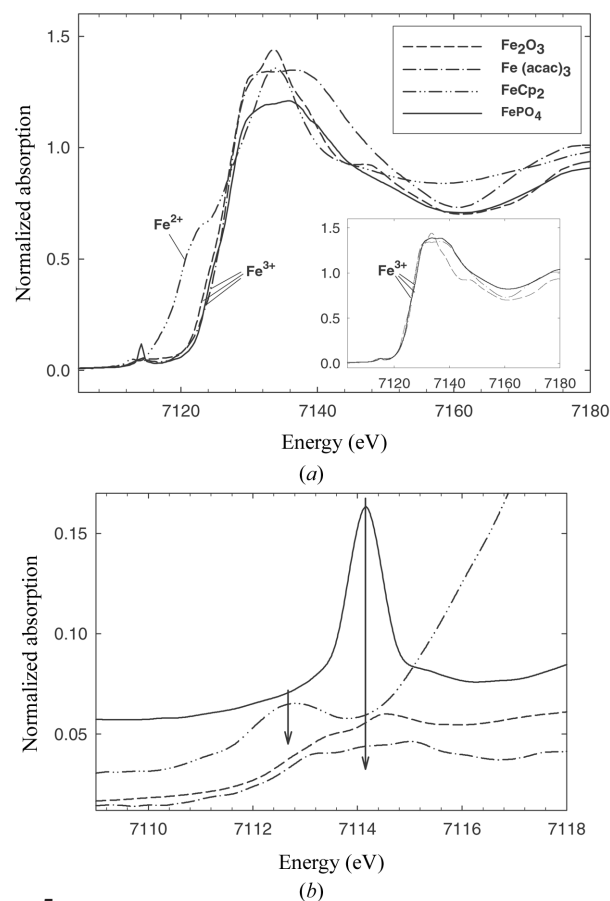(a) Calibrated and normalized XANES data at the Fe K edge during charge. A (0 mAh), B (0.75 mAh), C (1.50 mAh), D (2.25 mAh) and E (3.0 mAh) in the figure represent the different stages in the charge process at which the X-ray measurements were performed. (b) Pre-edge region of the XAS spectra, which shows the t_{2g} and e_g absorption bands at the stages A (LiFePO$_4$) and E (FePO$_4$).

Figure 5
(a) XANES spectra of the model compounds: Fe$_2$O$_3$ (short dash), Fe(acac)$_3$ (dash-dot), FeCp$_2$ (dash-dot-dot) and FePO$_4$ (solid line). The inset shows the comparison of the XANES spectrum recorded at stage E (solid line) with respect to the other Fe^{3+} model compounds, in octahedral symmetry [α-Fe$_2$O$_3$ (short dash) and Fe(acac)$_3$ (dash-dot)]. The axes in the inset are the same as in (a). (b) Magnified 1$s \rightarrow$ 3d pre-edge of XANES spectra for the model compounds. The different line codes are the same as in (a). The four spectra have been vertically shifted for clarity. The arrows represent the position of the pre-edge peaks.

photoelectric effect on a $1s$ electron is the oxidation state of the absorbing atom. Hence, more energy is required to ionize the deshielded metal ion with a higher electron deficit, and this explains the resulting consistent edge shift in the Fe(II) compounds with respect to the Fe(III) compounds considered here. This interpretation is also true for our observed edge shift in the charging process of the electrode from the initial state A [Fe(II)] to the final state E [Fe(III)] (Fig. 4a). By electrochemical delithiation during charging of the cell, the stoichiometry changes from Li_xFePO_4 to $FePO_4$, and, consequently, iron is oxidized from Fe(II) (stage A) to Fe(III) (stage E). The corresponding XANES for stage E was recorded approximately 3 h after the charging was started. The inset of Fig. 5(a) shows the XANES spectrum of this stage in comparison with the other model Fe(III) compounds (in octahedral symmetry). This comparison gives an independent confirmation of the assignment of state E ($FePO_4$) to Fe(III). It is important to note that $1s \rightarrow 3d$ pre-edge regions remain weak at the different stages of charging (Fig. 4b), indicating an approximately octahedral coordination. In contrast, the model compound with identical chemical composition ($FePO_4$) but in tetrahedral coordination shows a strong pre-edge (Fig. 5b). Furthermore, as seen in the figure, the $1s \rightarrow 3d$ pre-edge feature (Fig. 5b) is at slightly higher energy for Fe(III) compounds than for the Fe(II) compound. The pre-edge intensity of $FePO_4$ (in tetrahedral symmetry) is relatively intense (at 7114.1) with respect to Fe_2O_3 and Fe(acac)$_3$ (in octahedral symmetry), where in the case of the latter two compounds the pre-edge is split into two components of much lower intensity. For the Fe(III) compounds in octahedral symmetry, the relatively higher intensity observed for Fe_2O_3 results from the higher degree of distortion from the ideal octahedral symmetry with respect to Fe(acac)$_3$. Hence, the pre-edge feature represents the degree of mixing of the $3p$ and the $3d$ atomic orbitals to form molecular orbitals. In the case of a perfect O_h symmetry, the degree of mixing is zero leading to purely quadrupole transitions, but with increasing distortion of the O_h symmetry the orbitals acquire more p character. Finally, in the $FePO_4$ model compound with tetrahedral symmetry the pre-edge intensity is dominated by dipole transitions to orbitals with p character.

Another interesting feature of the XANES spectra reported here (Figs. 4 and 5) is the intensity of the white line, which is proportional to the coordination of the absorbing atom. The quantitative results obtained for the model compounds and the different states of charge for the Li_xFePO_4 electrode are summarized in Table 2. To briefly describe the interesting feature on the white lines of the measured XANES spectra, we observe that the white line intensities observed for the different states of charge (A, B, C, D and E) during charging of the *in situ* cell show a similar intensity to those observed for the other Fe(II) and Fe(III) [FeCp$_2$, α-Fe_2O_3, Fe(acac)$_3$] sixfold-coordinated (octahedral) model compounds (1.37–1.42; Table 2), much higher than that observed for the fourfold-coordinated (tetrahedral) model compound [$FePO_4$; 1.20]. This gives a phenomenological confirmation that, during charging of the *in situ* cell, iron in Li_xFePO_4 at different charged states remains in an octahedral coordination. Recently, Tang *et al.* (2003) performed a density functional calculation to study the electronic structure of $FePO_4$ and $LiFePO_4$. The calculations revealed that the spin polarization plays a vital role in stabilizing the electronic states. A comparison of different spin configurations confirmed that the ferromagnetic (high spin) configuration is the most stable configuration for both $FePO_4$ and $LiFePO_4$. There has also been an NMR study that predicts a high-spin configuration for $LiFePO_4$ (Tucker *et al.*, 2002). The Fe $3d$ states split into t_{2g} and e_g character and the Fermi level lies in the Fe $3d$ states. With deviation from the octahedral symmetry, interaction of the O $2p$ and

Table 2
Position and normalized intensity of the observed $1s \rightarrow 3d$ pre-edge peak and of the white line of the XANES for the different model compounds and for different states of charge of Li_xFePO_4 (A, B, C, D and E) during charging of the *in situ* cell.

(s) represents shoulder in the XANES spectra.

Sample or charged state	Pre-edge peak		White line	
	Position (eV)	Intensity	Position (eV)	Intensity
α-Fe_2O_3	7113.2 (s)	0.044	7133.6	1.42
	7114.4	0.058		
Fe(acac)$_3$	7113.3 (s)	0.042	7132.9	1.41
	7114.9	0.046		
FeCp$_2$	7112.8	0.051	7133.8	1.40
$FePO_4$	7114.1	0.125	7136.1	1.20
A (0.0 mAh)	7113.3	0.054	7129.2	1.41
B (0.75 mAh)	7113.8	0.053	7130.2	1.38
C (1.5 mAh)	7114.4	0.053	7131.2	1.38
D (2.25 mAh)	7114.9	0.053	7132.3	1.37
E (3.0 mAh)	7115.4	0.055	7133.4	1.39

Fe $3d$ orbitals causes further splitting of these states. As discussed above, the mixing of the O $2p$ and the Fe $3d$ orbitals increases the transition probability of the $1s \rightarrow 3d$ transition (which is dipole forbidden). As the e_g orbitals overlap better with the $2p$ orbitals, the transition probability to e_g states would be higher. In the case of $FePO_4$ (Fe^{3+}, d^5) it would be more pronounced as the e_g states are less occupied compared with the Fe(II) compound. The expected low- and high-spin electronic configurations of Fe(II) (assuming octahedral oxygen coordination around iron) are shown in Fig. 6, together with the X-ray absorption transitions at the Fe K edge.

We will now discuss structural changes during charging of the cell by focusing mainly on the starting state A (0 mAh) and the oxidized electrode sample at state E (3 mAh). Reduction of the absorption data was performed using *EXAFSPAK*. First the transmission data from the scans were averaged and the background was subtracted. The spectra were normalized using a quartic spline fit through the background and the resulting $\chi(k)$ function was then weighted with k^3 in order to emphasize the high k-region of the data where the
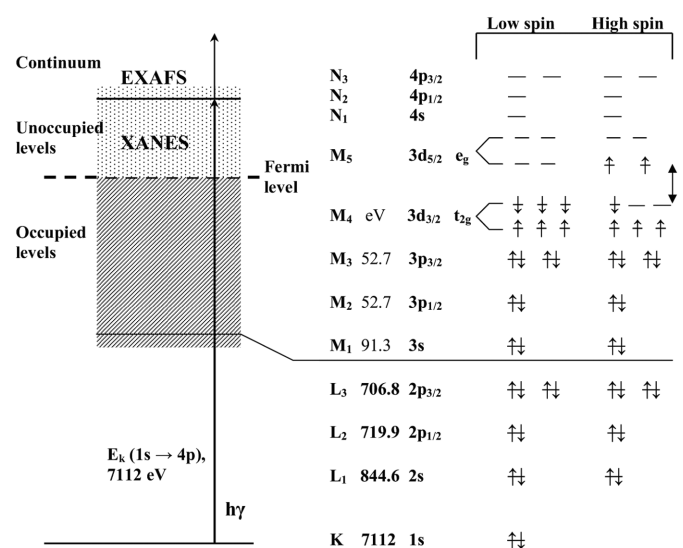

Figure 6
The XAS process and the electronic configuration of the Fe^{2+} ion and possible transitions, depicting the high-spin configuration in $LiFePO_4$ (assuming octahedral coordination of the O atoms). The arrow ($\updownarrow$) here shows the observed transitions ($\sim$2 eV) to the XANES (Fig. 4b), in the high-spin configuration in $LiFePO_4$.

Table 3
Structural parameters resulting from the FEFF fit for Li_xFePO_4 during the initial stage A (0 mAh), derived from fitting the Fe-edge EXAFS spectra.

Numbers in parentheses are statistical errors of the last significant digit. Z_a–Z_b represents the central absorber and the scattering atom (or path) correlation, CN is the coordination number, R is the interatomic distance, σ^2 represents the Debye–Waller disorder parameter. k range = 1.5–16.2 Å^{-1}.

Sphere	Z_a–Z_b	CN	R (Å)	σ^2 (Å^2 × 10^{-3})
1st	Fe—O	2	1.991 (2)	1.2 (4)
1st	Fe—O	2	2.122 (3)	2.4 (5)
1st	Fe—O	2	2.264 (5)	4.8 (7)
2nd	Fe—P	1	2.799 (5)	1.8 (1)
2nd	Fe—P	2	3.179 (6)	4.1 (3)
2nd	Fe—P	2	3.299 (2)	6.3 (3)
3rd	Fe—Fe	2	3.813 (2)	4.5 (2)
3rd	Fe—Fe	2	4.187 (6)	6.2 (5)

Table 4
Structural parameters resulting from the FEFF fit for Li_xFePO_4 during the fully charged stage E (3.0 mAh), derived from fitting the Fe-edge EXAFS spectra.

Numbers in parentheses are statistical errors of the last significant digit. Z_a–Z_b represents the central absorber and the scattering atom (or path) correlation, CN is the coordination number, R is the interatomic distance, σ^2 represents the Debye–Waller disorder parameter. k range = 1.5–16.2 Å^{-1}.

Sphere	Z_a–Z_b	CN	R (Å)	σ^2 (Å^2 10^{-3})
1st	Fe—O	2	1.793 (5)	1.5 (4)
1st	Fe—O	2	1.996 (8)	2.2 (5)
1st	Fe—O	2	2.201 (5)	4.0 (7)
2nd	Fe—P	1	2.793 (7)	1.7 (1)
2nd	Fe—P	2	3.177 (3)	4.3 (3)
2nd	Fe—P	2	3.186 (7)	6.1 (3)
3rd	Fe—Fe	2	3.794 (2)	4.2 (2)
3rd	Fe—Fe	2	4.166 (6)	6.5 (5)

theory is most accurate, and to negate the amplitude reductions. The radial structure function was obtained by Fourier transformation of $k^3\chi(k)$ using a k range from 1.5 to 16.2 Å^{-1}. This k range was chosen to obtain a Fourier transform with no spurious peaks below the anticipated lowest Fe—O distance. Finally, a fit to the EXAFS spectrum was made with theoretical scattering paths, which were generated with the *FEFF8* code (Ankudinov *et al.*, 1998). Fig. 7(*a*) shows the *k*-weighted EXAFS spectra recorded during the charging of the cell at stages A and E when the Fe oxidation state was (II) and (III), respectively. The corresponding Fourier transforms of $k^3\chi(k)$ are shown in Fig. 7(*b*). The radial structure function at the two stages A and E shows one strong peak at the start followed by two weaker peaks at higher distances. The peak positions in this radial structure function are close to the radius of the back-scattering shells. Quantitative analyses were performed on the first three peaks appearing in the radial structure function between $R = 0.5$ and 4.1 Å. The structural parameters shown in Tables 3 and 4 are obtained from the FEFF fit analysis of Li_xFePO_4 using all possible scattering paths. The coordination numbers (CN) were fixed, while the distance (R), Debye–Waller factors (σ^2) and shift from E_0 were left as free parameters. The coordination atom of the first shell is oxygen, and that of the second and the third shells are phosphorous and iron, respectively. The best fit was obtained by assuming three different Fe—O distances as shown in Tables 3 and 4. The Fe—O distances obtained for the two stages A and E varied at most by 0.2 Å. Using four Fe—O scattering paths did not improve the fit substantially. The best fit was obtained with three Fe—O distances and is shown here. The second peak corresponds to the single-scattering paths of Fe—P, corresponding to those obtained from the XRD data as shown in Table 1, in the case of stage A. This is similar to that obtained for the charged

stage E, while the Fe—P scattering distances varied at the most by 0.1 Å. Comparing stages A and E (Figs. 7*a* and 7*b*) reveals that only subtle changes take place, the structural rearrangement on lithium extraction in Li_xFePO_4 is small, as seen from Tables 3 and 4, and the change in Fe—O coordination is minimal: the mean Fe—O distances are 2.13 and 2.01 Å for $LiFePO_4$ and $FePO_4$, respectively. As pointed out above, no single Fe—O distance varies by more than 0.2 Å. This again shows the basis for the truly excellent cycling properties for this system. The results obtained for both stages A and E are in agreement with the crystallographic data, which reported that $FePO_4$ (at stage E) retains the same *Pnma* structure, and there is a 7% reduction in volume. The electrochemical data (very flat discharge and charge voltage plateaus) taken together with the XAS results indicate that the $LiFePO_4$ electrode functions as a two-phase system, with $FePO_4$ in equilibrium with $LiFePO_4$. Thus, the XAS spectra for the intermediate compositions can be represented as a linear combination of the two single-phase spectra. This is shown in Fig. 8 as a two-component fit of state A (0.0 mAh) and state E (3.0 mAh) for the intermediate compositions at states B, C and D, respectively. State B is seen to be composed of 66.3% of state A and 33.7% of state E, state C is composed of 56.1% of state A and 43.9% of state E, while state D is composed of 33.6% of state A and 66.4% of state E.
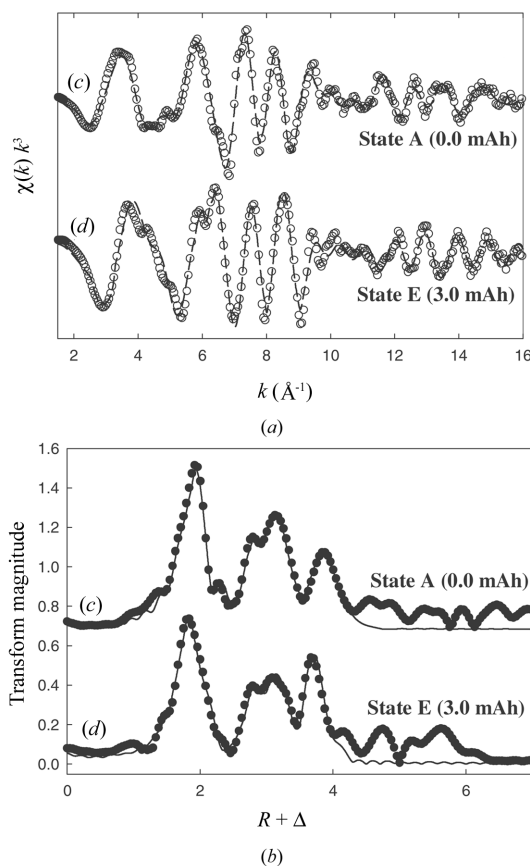

Figure 7
(*a*) Comparison between the experimental and the FEFF fit theoretical analysis of the k^3-weighted [$k^3\chi(k)$] Fe EXAFS spectrum of (*c*) Fe(II) recorded at the state A and (*d*) Fe(III) recorded at the state E, for Li_xFePO_4 during charging. For both (*c*) and (*d*), circles indicate experimental data and broken lines indicate FEFF fit theoretical results. (*b*) Comparison of the radial distribution function obtained after Fourier transformation of $k^3\chi(k)$ observed at state A and state E. For both (*c*) and (*d*), circles (filled) indicate experimental data and solid lines indicate FEFF fit theoretical results.
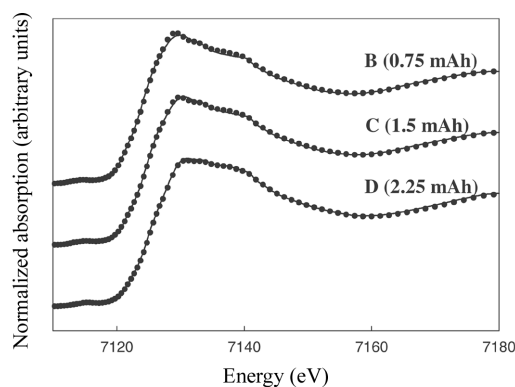
Figure 8
The two-component (states A and E) fit for the intermediate states B (0.75 mAh), C (1.5 mAh) and D (2.25 mAh). The experimental spectra are represented by filled circles and the fit results are represented by solid lines. State B is represented by a fit with concentrations of state A (0.663) and state E (0.337); state C is represented by state A (0.561) and state E (0.439); state D is represented by state A (0.336) and state E (0.664).

5. Conclusion

An XAS characterization of Li_xFePO_4-based electrode material during the charging cycle has been performed. The study was made possible by using a versatile novel *in situ* cell, particularly designed for long time transmission X-ray experiments. The cell contains a lithium metal counter/reference electrode and can operate safely for more than seven days without any significant traces of corrosion. XAS has provided us with an excellent tool for analyzing the changes that take place when Li is cycled out of and into Li_xFePO_4 in a Li-ion cell. The XAS results indicate that during charging of Li_xFePO_4 to 4 V the oxidation state of Fe changes from (II) to (III) with the retention of the Fe—O octahedral symmetry. This result confirms that the material possesses very desirable characteristics for an electrode, which makes it an excellent choice for Li-ion cell applications. This assignment was obtained by comparison of the XANES pre-edge intensities with the model compounds. The pre-edge intensities at the different states of charge of Li_xFePO_4 show that the octahedral arrangement of the phosphate O atoms around each Fe site is retained. XANES studies revealed furthermore that the LiFePO4 and FePO4 are both in the expected high-spin state and exhibit a crystal field splitting of about 2 eV. The EXAFS data show one strong peak for the first coordination shell corresponding to Fe—O scattering contributions, and two weaker peaks at higher distances comprise of contributions from Fe—P and Fe—Fe, respectively. The change in R_{Fe-O} from the initial stage A (0.0 mAh) [LiFePO4] to the fully charged state E (3 mAh) [FePO4] varies by ≤ 0.2 Å, confirming that only minor changes occur in the structure of the electrode during electrochemical cycling. The electrochemical results taken in combination with the XAS results indicate that the LiFePO4 electrode operates as a two-phase electrode, exhibiting a very stable potential during both charge and discharge.

References

Andersson, A. S. & Thomas, J. O. (2001). *J. Power Sources*, **97/98**, 498–502.
Ankudinov, A. L., Ravel, B., Rehr, J. J. & Conradson, S. D. (1998). *Phys. Rev. B*, **58**, 7565–7576.
Bianconi, A. (1988). *X-ray Absorption*, edited by D. C. Koningsberger, Vol. 1, p. 573. New York: Wiley.
Chung, S. Y., Blocking, J. T. & Chiang, Y.-M. (2002). *Nature Mater.* **1**, 123–128.
Doeff, M. M., Hu, Y., McLarnon, F. & Kostecki, R. (2003). *Electrochem. Solid State Lett.* **6**, A207–209.
Eiland, P. F. & Pepinsky, R. (1952). *J. Am. Chem. Soc.* **74**, 4971.
Etgens, V. H., Alves Martins, M. C. & Tadjeddine, A. (1999). *Electrochem. Acta*, **45**, 591–599.
Frahm, R. (1988). *Nucl. Instrum. Methods Phys. Res. A*, **270**, 578–581.
Gerand, B., Blyr, A., Pasquier, Du A., Leriche, J. B. & Seguin, L. (1999). *J. Power Sources*, **81/82**, 922–924.
Haas, O. & Cairns, E. J. (1999). *Annu. Rep. Prog. Chem. Sect. C*, **95**, 163–165.
Huang, K., Lee, H. Y. & Goodenough, J. B. (1998). *J. Electrochem. Soc.* **145**, 3220–3227.
Manceau, A., Drits, V. A., Lanson, B., Chateigner, D., Wu, J., Huo, D., Gates, W. P. & Stucki, J. W. (2000). *Am. Miner.* **85**, 153–172.
Mansour, A. N., McBreen, J. & Melendres, C. A. (1999). *J. Electrochem. Soc.* **146**, 2799–2809.
Newville, M. (2001). *J. Synchrotrron Rad.* **8**, 322–324.
Ng, H. N. & Calvo, C. (1975). *Can. J. Chem.* **53**, 2064–2068.
Padhi, A. K., Nanjundaswamy, K. S. & Goodenough, J. B. (1997). *J. Electrochem. Soc.* **144**, 1188–1194.
Palacin, M. R., Cras, F. Ie., Seguin, L., Anne, M., Chabre, Y., Tarascon, J. M., Amatucci, G., Vaughan, G. & Strobel, P. (1999). *J. Solid State Chem.* **144**, 361–371.
Pouchard, M., Villesuzanne, A. & Doumerc, J.-P. (2001). *J. Solid State Chem.* **162**, 282–292.
Ravet, N., Chouinard, Y., Magnan, J. F., Besner, S., Gautier, M. & Armand, M. (2001). *J. Power Sources*, **97/98**, 503–507.
Richard, M. N., Koetschau, I. & Dahn, J. R. (1997). *J. Electrochem. Soc.* **144**, 554–557.
Ronci, F., Scrosati, B., Albertini, V. R. & Perfetti, P. (2001). *J. Phys. Chem. B*, **105**, 754–759.
Segre, C. U., Leyarovska, N. E., Lavender, W. M., Plag, P. W., King, A. S., Kropf, A. J., Bunker, B. A., Kemner, K. M., Dutta, P., Duran, R. S., Kaduk, J. (2000). *CP521, Synchrotron Radiation Instumentation: 11th US National Conference*, edited by P. Pianetta *et al.*, p. 419 New York: American Institute of Physics.
Streltsov, V. A., Belokoneva, E. L., Tsirelson, V. G. & Hansen, N. K. (1993). *Acta Cryst.* B**49**, 147–153.
Tang, P. & Holzwarth, N. W. A. (2003). *Phys. Rev. B*, **68**, 165107.
Tucker, M. C., Doeff, M. M., Richardson, T. J., Finones, R. & Cairns, E. J. (2002). *J. Am. Chem. Soc.* **124**, 3832–3833.
Westre, T. E., Kennepohl, P., DeWitt, J. G., Hedman, B., Hodgson, K. O. & Solomon, E. I. (1997). *J. Am. Chem. Soc.* **119**, 6297–6314.
Yakubovich, O. Y. V., Simonov, O. V. & Belov, N. V. (1977). *Sov. Phys. Dokl.* **22**, 347–352.
Yamada, A. & Chung, C.-S. (2001). *J. Electrochem. Soc.* **148**, A960–967.
Yamada, A., Chung, S. C. & Hinokuma, K. (2001). *J. Electrochem. Soc.* **148**, A224–229.
Yang, S., Song, Y., Ngala, K., Zavalli, P. Y. & Whittingham, M. S. (2003). *J. Power Sources*, **119/121**, 239–246.
Yang, S., Song, Y., Zavalli, P. Y. & Wittingham, M. S. (2002). *Electrochem. Commun.* **4**, 239–244.